J. Meas. Sci. Instrum., 2024, 15(2): 157-165.
DOI: 10.62756/jmsi.1674-8042.2024016
http://jmsi.publish.founderss.cn/
jmsi@nuc.edu.cn

Solution of light vector superposition heading in zenith region of underwater sky polarization image

FANG Zheng[1], GUO Yinjing[1,2*], KONG Fang[3], LÜ Xue[1], DU Chunxiao[1], RUAN Yaohuang[1]

1.School of Electronic and Information Engineering, Shandong University of Science and Technology, Qingdao 266590, China;
2.Qingdao Zhihai Muyang Technology Co., Ltd., Qingdao 266590, China;
3. School of Electrical and Automation Engineering, Shandong University of Science and Technology, Qingdao 266590, China

***Corresponding author:** GUO Yinjing (gyjlwh004@126.com)

Received: March 6, 2024 **Revised:** April 16, 2024 **Accepted:** May 17, 2024

Abstract: Underwater skylight polarization images can be utilized for heading measurement, offering advantages such as anti-interference and no accumulation error. A method for underwater polarization image heading estimation was presented based on the superposition of light vectors in the zenith region, with the aim of obtaining the heading angle in underwater environments. The polarization information from the zenith region was analyzed and extracted in conjunction with attitude information. Subsequently, the underwater refracted light polarization vector was synthesized with the atmospheric polarization light vector within the zenith region using superposition operations. Through optimization of the polarization vector, the heading angle of underwater targets was accurately determined. Experimental results demonstrated that the root mean square error (RMSE) of the heading angle in the proposed method was 0.30° in the tank experiment and 0.41° in the marine experiment. Moreover, in the oceans at depths of 0.98 m, 4.89 m, and 5.94 m, the RMSE of the solar azimuth was 1.10°, 2.03°, and 3.04°, respectively.

Key words: polarization images; heading measurements; zenith region; vector superposition

0 Introduction

Underwater navigation and positioning pose significant challenges in fields such as marine engineering, underwater archaeology, underwater resource development, and marine science[1,2]. Due to the complexity and challenges of underwater environments, designing effective underwater navigation and positioning systems is crucial. These systems mainly rely on technologies such as sonar, inertial navigation, GPS[3], and geomagnetic navigation. However, these technologies face limitations in the underwater environment.

Sonar technology mainly rely on the propagation and reflection characteristics of sound for localization. However, sound is easily influenced by various factors during its propagation, such as obstacles, the selection of sound frequency and amplitude, the directionality of sound waves, interference, and noise. These factors may lead to inaccurate positioning results[4]. Inertial navigation systems are affected by integration drift issues, and long-term operation results in the accumulation of measurement errors[5]. GPS signals propagate through radio waves, and most of them can not penetrate water layers. When GPS signals hit the water, most of them are reflected back into the air rather than continuing to travel through the water layer[6]. The strength of the geomagnetic field is relatively weak and susceptible to interference from other magnetic field sources. Additionally, the distribution of the geomagnetic field is not uniform, with regional differences and variations[6].

In recent years, significant progress is made in the field of atmospheric polarized light navigation. A direction-solving model called POL-ANN was proposed by Wang et al.[7]. A convolutional operation method for removing occlusions was introduced[8,9]. The symmetry of polarization angle images was utilized by Zhao et al. to extract the solar meridian for heading estimation[10]. Calibration of biomimetic polarized orientation sensors was conducted by Wan et al., resulting in improved accuracy in heading measurements[11]. While significant progress has been made in atmospheric polarized light navigation, underwater environments present a series of

unique challenges and opportunities.

Underwater skylight polarization imaging is used for underwater navigation by utilizing information from the polarization of light in the underwater sky. It has broad prospects for applications. Research on underwater polarized light began in 1954 when Waterman discovered that light in the ocean was predominantly linearly polarized. In 1958, a further study confirmed that skylight maintained 40% polarization even at a depth of 100 m underwater, after passing through the water surface[12]. Powell et al. took into account the effects of direct refraction of sunlight through the water surface and single scattering under the water, and they established an underwater polarization transmission model to predict the polarization distribution under the water[13]. Mantis shrimp[14] and rainbow trout[15] can sense polarized light and use it for predation. Sabbah et al. utilized stokes vectors and Mueller matrices to simulate the underwater polarization distribution after refraction at a static air-water interface[16].

Snell window is a phenomenon of reducing the sky view caused by light refraction during underwater observation[17]. Hu et al. constructed an underwater polarization compass within a water tank[18]. The results showed that the intensity of polarized light inside the window was higher than that outside the window, which helped to improve the accuracy of determining the sun's position. Additionally, an underwater sun tracking algorithm was developed, and heading calculations utilized the central data within the snell window. The 3D CoHT method was adopted by Yang et al. to extract horizontal attitude information from the snell window[19]. A method for autonomous localization, known as the LIG method, was proposed by Hu et al.[20], which was based on the underwater light intensity gradient field and improved the environmental adaptability of underwater light field navigation. LIG utilized the spatial information contained in the light intensity field and converted the scalar field of light intensity into a vector field through gradient calculations. Dupeyroux proposed a single-pixel point polarization-based direction finding method and conducted polarization-based orientation experiments in clear shallow water, achieving results comparable to ground-based measurements[21]. It is also suggested that maintaining the horizontal orientation of the detection device is essential for conducting polarization orientation underwater. To address this limitation, a common approach is to integrate the polarimeter with an inertial navigation module[22].

When the sensor is tilted, the central area of the snell window no longer corresponds to the zenith area, causing the selected sky region to continuously change in dynamic situations. This makes it difficult for the polarized light compass to establish a consistent heading reference when tilted, thereby affecting the accurate acquisition of heading information. Based on the $\boldsymbol{E}$ vector method, heading error can be explained as the result of the combined effect of accuracy loss during zenith point tracking and atmospheric refraction effect.

In order to address the limitations of keeping the acquisition sensor horizontal and the error loss in the $\boldsymbol{E}$ vector method, the method proposed in this study addressed this challenge with innovation, primarily through the horizontal adaptive filtering of the zenith region using an underwater polarized light compass, while considering the refraction of sunlight through surface scattering. The key innovations could be briefly summarized as follows: 1) Adaptive filtering of zenith area: To address the issue of variable zenith area due to sensor tilt, a horizontally adaptive filtering method was proposed to ensure that the selected area still effectively corresponded to the zenith area. 2) Considering underwater refraction and atmospheric polarization: The polarization vector superposition calculation was introduced for underwater refraction and atmospheric polarization. By considering these two components, a more comprehensive modeling of light propagation in underwater environments was achieved.

This method not only mitigated the influence of horizontal attitude angles but also provided more accurate heading information in underwater environments. By intelligently filtering the zenith region and comprehensively processing the polarized light composed of refracted light, it partially overcame the limitations of traditional methods under tilted conditions.

1 Design of algorithm

A camera-based polarimeter was employed in which the image sensor chip comprised of four polarization sensing units oriented in four different directions (0°, 45°, 90°, and 135°), arranged in a matrix pattern. The raw data obtained for each photoreceptor unit were denoted as I_0, I_{45}, I_{90}, and I_{135}, respectively, which could be utilized to compute both the intensity and polarization information. Among them, the polarization directions of 0°, 45°, 90°, and 135° respectively indicated that the vibration direction of light was in the horizontal direction, at a 45° angle to the horizontal direction, in the vertical direction, and at a 135° angle to the horizontal direction. Using this data, the first three Stokes

parameters are reconstructed as follows: S_0, S_1, and S_2 represent the total intensity of the light wave, the linearly polarized light components in the horizontal and vertical directions, and the linearly polarized light components in the 45° and 135° directions, respectively. S_3 represents the right-handed and left-handed circularly polarized light components, set to 0 here.

$$\begin{cases} S_0 = 0.5(I_0 + I_{45} + I_{90} + I_{135}), \\ S_1 = I_0 - I_{90}, \\ S_2 = I_{45} - I_{135}, \\ S_3 = 0. \end{cases} \tag{1}$$

The azimuthal angle of the observation direction of the image-based underwater polarized sensor was denoted as ψ_p, with the polarization angle (AoP) relative to the 0° polarizer being ψ_{p0}.

$$\psi_{p0} = 0.5\text{atan2}(S_2, S_1) - b - \frac{\pi}{2}, \tag{2}$$

where b is the angle between the 0° polarizer and the local meridian[23].

$$\psi_p = \begin{cases} \psi_{p0} + \pi, & \psi_{p0} < -\dfrac{\pi}{2}, \\ \psi_{p0} - \pi, & \psi_{p0} > \dfrac{\pi}{2}. \end{cases} \tag{3}$$

To convert the underwater polarization distribution to the atmospheric polarization distribution, it is necessary to first select pixels within the zenith region of the snell window. To mitigate the errors caused by the inclination of imaging devices, it is necessary to extract the center point and radius of the zenith region based on the attitude angles of the underwater device, namely pitch angle (α), roll angle (γ), and yaw angle (δ). The tilt angle (β) is the angle between the optical axis of an underwater polarized camera and the horizontal direction, calculated using trigonometric relationships with the attitude angles α and γ.

$$\beta = \arccos(\cos\alpha \cos\gamma). \tag{4}$$

Identify the center point (X_c, Y_c) of the required zenithal region, that is

$$(X_c, Y_c) = \begin{cases} \dfrac{h}{2}(1 + \tan\beta \sin\delta), \\ \dfrac{w}{2}(1 - \tan\beta \sin\delta), \end{cases} \tag{5}$$

where h is the height of the image, and w is the width of the image. The radius of the zenith area can be calculated by

$$r = \frac{d}{2}\left(\frac{\pi}{2} - \frac{FOV}{2} - \beta\right), \tag{6}$$

where d represents the diagonal length of the polarized image, and FOV denotes the field of view of the polarized camera.

The effective range of the zenithal region is

$$\sqrt{(i - X_c)^2 + (j - Y_c)^2} \leqslant r, \tag{7}$$

where (i, j) represents the coordinates of a pixel, and r is taken as the absolute value.

In the polarization imaging device, it is necessary to ensure the observation of the zenith region in the image when tilted. Therefore, the maximum values of α and γ should satisfy[24]

$$\alpha_{max} = \gamma_{max} = \frac{FOV}{2} - m, \tag{8}$$

where m represents the region of interest.

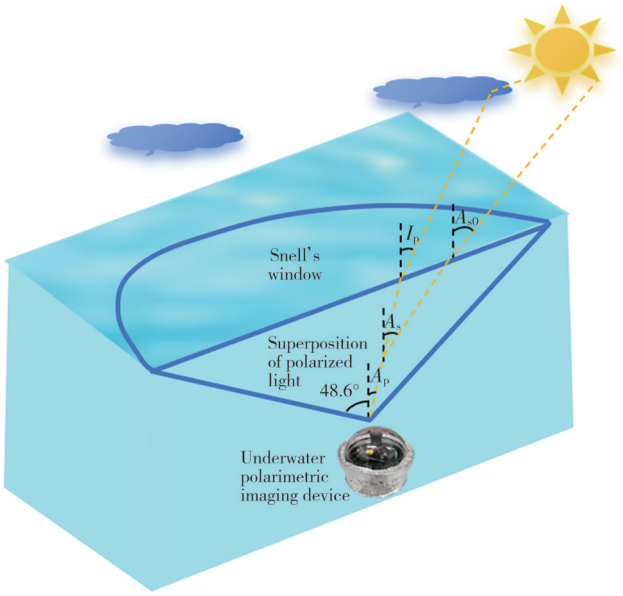

Fig. 1 Schematic diagram of polarized light propagation at air water interface

The $\boldsymbol{E}$ vector referred to the electric field vector, which determined the polarization state of light. The incident electric field vector could be decomposed into two orthogonal components, one perpendicular ($\boldsymbol{E}_\perp$), and one parallel ($\boldsymbol{E}_\parallel$) to the plane of incidence. According to the Fresnel transmission law, for the incident and transmitted polarized light amplitudes $\boldsymbol{E}_\perp$, $\boldsymbol{E}'_\perp$, $\boldsymbol{E}_\parallel$ and $\boldsymbol{E}'_\parallel$ parallel and perpendicular to the plane of incidence, the relations before and after refraction is

$$\begin{cases} \dfrac{\boldsymbol{E}'_\parallel}{\boldsymbol{E}_\parallel} = \dfrac{2n_a \cos I_p}{n_w \cos I_p + n_a \cos A_p}, \\ \dfrac{\boldsymbol{E}'_\perp}{\boldsymbol{E}_\perp} = \dfrac{2n_a \cos I_p}{n_a \cos I_p + n_w \cos A_p}. \end{cases} \tag{9}$$

The zenith position in the zenith region was taken as the reference solar position. The zenith angle of the observation direction of the underwater polarization sensor, denoted as A_p, and the underwater reference

solar zenith angle, denoted as A_s, can be determined through the camera geometric model[25].

The atmospheric polarization azimuth P^{air} and ψ_p can be calculated from the definition of the polarization azimuth.

$$\tan p^{air}=\frac{E_{\perp}}{E_{\parallel}},\ \tan\psi_p=\frac{E'_{\perp}}{E'_{\parallel}}. \tag{10}$$

Fig.2 illustrates the sky polarization distribution model based on the Rayleigh scattering model. Where S is the position of the sun, P is the sky observation point, and H_s is the solar altitude angle, ψ_s is the sun's azimuth in the carrier coordinate system, ψ_{s0} is the underwater sun azimuth angle, and ψ is the heading angle. It is worth noting that the range of zenith angle values is $[0°, 90°]$, and the range of azimuth angle values is $[-180°, 180°]$. $O_i-X_iY_iZ_i$ is incident light coordinate system. Y_i axis is omitted in the figure. $O_b-X_bY_bZ_b$ is carrier coordinate system (i.e., camera coordinate system). $O_n-X_nY_nZ_n$ is navigation coordinate system, where the O_n point coincides with the O_b point, the X_n axis points due north, and Z_n and Z_b coincide. The Y_n and Z_n axes are omitted from the diagram.

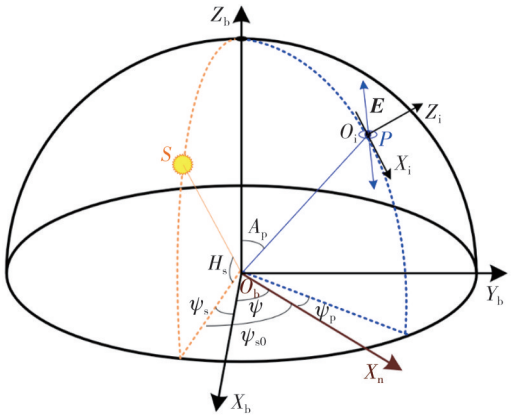

Fig. 2 Rayleigh scattering model diagram

The azimuth angle of polarized light in the atmosphere, denoted as P^{air}, is obtained by

$$P^{air}=\arctan\left(\frac{n_a\cos I_p+n_w\cos A_p}{n_w\cos I_p+n_a\cos A_p}\tan\psi_p\right), \tag{11}$$

where I_p represents the angle of incidence in the atmosphere, $I_p=\arcsin\left(\frac{n_w}{n_a}\sin A_p\right)$, where n_w is the refractive index of water and n_a is the refractive index of air.

According to Rayleigh scattering theory, the polarization azimuth angle of the underwater refracted light formed by sunlight incidence is[26].

$$P^{sca}=\arctan\left(\frac{\cos A_s\sin A_p-\sin A_s\cos A_p\cos(\psi_{s0}-\psi_p)}{\sin A_s\sin(\psi_{s0}-\psi_p)}\right). \tag{12}$$

The polarization vector can be obtained by superimposing the atmospheric polarized light vector with the underwater refracted light vector, as shown in Fig.3. The polarization vector of atmospheric polarized light is represented as $\boldsymbol{E}^{air}$, while the polarization vector of underwater refracted light is represented as $\boldsymbol{E}^{sca}$. In the coordinate system of incident light, the definitions are

$$\begin{cases}\boldsymbol{E}^{air}=\begin{bmatrix}\cos P^{air} & \sin P^{air} & 0\end{bmatrix}^{\mathrm{T}},\\ \boldsymbol{E}^{sca}=\begin{bmatrix}\cos P^{sca} & \sin P^{sca} & 0\end{bmatrix}^{\mathrm{T}}.\end{cases} \tag{13}$$

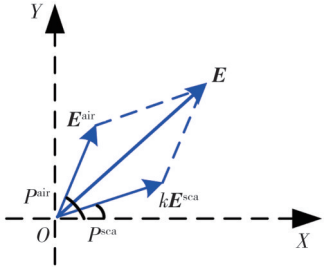

Fig. 3 Schematic diagram of superposition of atmospheric polarization vector and underwater refraction polarization vector

The polarization vector $\boldsymbol{E}$ formed by the superposition of atmospheric polarized light and underwater refracted light is

$$\boldsymbol{E}=\boldsymbol{E}^{air}+k\boldsymbol{E}^{sca}. \tag{14}$$

The weight factor k is

$$k=\frac{\sin(\psi_p-P^{air})}{\sin(P^{sca}-\psi_p)}. \tag{15}$$

In the coordinate system $O_i-X_iY_iZ_i$ at the sky observation point, the synthesized polarized vector is the polarized vector $\boldsymbol{E}$ at the point P, which is represented as

$$\boldsymbol{E}=\begin{bmatrix}\cos P^{air}+k\cos P^{sca} & \sin P^{air}+k\sin P^{sca} & 0\end{bmatrix}^{\mathrm{T}}. \tag{16}$$

$\boldsymbol{R}_i^b$ refers to the coordinate transformation matrix from the sky observation point coordinate system to the carrier coordinate system.

$$\boldsymbol{R}_i^b=\begin{bmatrix}\cos\psi_p\cos A_p & -\sin\psi_p & \cos\psi_p\sin A_p\\ \sin\psi_p & \cos\psi_p & \sin\psi_p\sin A_p\\ -\sin A_p & 0 & \cos A_p\end{bmatrix}. \tag{17}$$

The polarization vector $\boldsymbol{E}_n$ in the carrier coordinate system can be expressed as

$$\boldsymbol{E}_n=\boldsymbol{R}_i^b\boldsymbol{E}=\begin{bmatrix}\cos\psi_p\cos A_p(\cos P^{air}+k\cos P^{sca})-\sin\psi_p(\sin P^{air}+k\sin P^{sca})\\ \sin\psi_p\cos A_p(\cos P^{air}+k\cos P^{sca})+\cos\psi_p(\sin P^{air}+k\sin P^{sca})\\ -\sin A_p(\cos P^{air}+k\cos P^{sca})\end{bmatrix}. \tag{18}$$

When calculating the solar vector, P^{air} of pixel polarized vectors for cross-product operation was seclected to obtain the solar vector $\boldsymbol{s}$[18]. In the carrier coordinate system, ψ_s is calculated by

$$\psi_s = \frac{180}{\pi}\operatorname{atan2}\big(\boldsymbol{s}(2),\boldsymbol{s}(1)\big). \tag{19}$$

When the observation time and longitude and latitude of the observation point are known, astronomical knowledge can be used to calculate the solar altitude angle H_s and azimuth angle ψ_{s0}, where ψ_{s0} is the angle of counterclockwise rotation with zero degrees in the north direction[27].

$$H_s = \arcsin(\sin Lat \sin c + \cos Lat \cos c \cos H), \tag{20}$$

where H represents the solar hour angle; Lat denotes the latitude of the observation point; and c stands for the solar declination angle.

$$\psi_{s0} = \arccos\left(\frac{\sin Lat - \cos H_s \sin c}{\sin H_s \cos c}\right). \tag{21}$$

The calculation method of the heading angle is[25]

$$\psi = \psi_{s0} - \psi_s, \text{ or } \psi = \psi_{s0} - \psi_s + \pi. \tag{22}$$

To better illustrate the complex steps and internal relationships of the algorithm, the algorithm flow is shown in Fig.4.

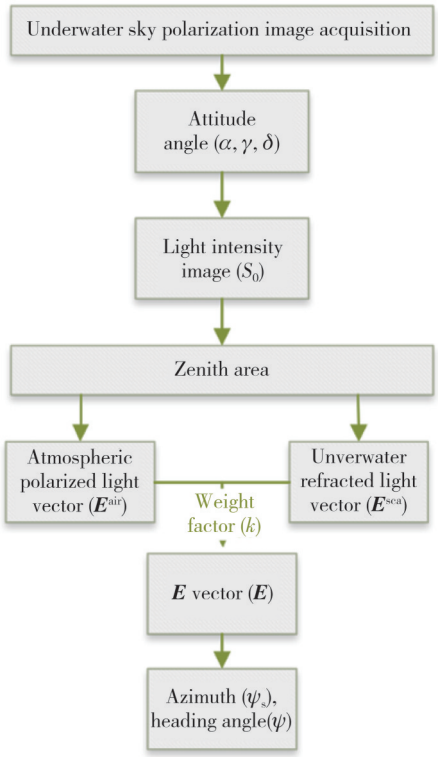

Fig. 4 Algorithm flow chart

2 Experiment

2.1 Experimental setup design

The design of the hardware system encompasses multiple key components, as shown in Table 1. Fig. 5 illustrates the experimental setup and environment. Waterproof measures included external coverage with waterproof tape and internal iron cylinders, approximately 24.1 cm in diameter and 12.5 cm in height. The transparent shell above was made of polymethyl methacrylate, with a central height of approximately 11.3 cm. The system integrated a Sony IMX264MZR polarized camera (equipped with a fisheye lens), an N100MINI inertial navigation module produced by Wheeltec, a water level sensor, a self-made control motherboard, and optical fiber transceivers. The bottom was equipped with an MS5837 depth sensor, and the circuit came out of the reserved through hole at the bottom.

Table 1 Equipment required for experiment

Equipment	Quantity
PC	1
Sony IMX264MZR polarized camera	1
FE185C057HA-1 fisheye lens	1
Custom-made waterproof housing	1
Self-made main control board	1
12 V mobile power supply	1
N100MINI inertial navigation module	1
MS5837 depth sensor	1
Water level sensor	1
Optical fiber transceiver	1
Solid-state drive	1
5 kg weight	1

A polarization camera was connected to a PC via an optical fiber transceiver, responsible for capturing polarized images of underwater sky light at 0°, 45°, 90°, and 135°, and saving the image information to the solid-state hard drive connected to the PC for subsequent processing. The portable power supply adjusted and stabilized the output voltages to 3.3 V, 5 V, and 12 V, respectively, providing the necessary power for the normal operation of each module. The MS5837 depth sensor continuously monitored the depth and pressure information of the system in real-time via the IIC protocol to prevent excessive environmental pressure. The water level sensor was utilized to detect the airtightness of the waterproof casing, thus preventing damage to the system.

The N100MINI monitored the system's attitude information and communicated it to the control mainboard via the SPI communication protocol. Quantity represents the quantity used in the Table 1.

The original image size obtained by the polarized camera was 2 048×2 448 pixels, consisting of I_0, I_{45}, I_{90}, and I_{135}. In the experiment, exposure time was automatically adjusted according to different light intensities. The ROI-A method proposed in this paper was compared with the simulated results of ROI-A (SimROI-A), the method by Wang et al.[28], the method by Xu et al.[29], and the baseline angle measured using the N100MINI module.

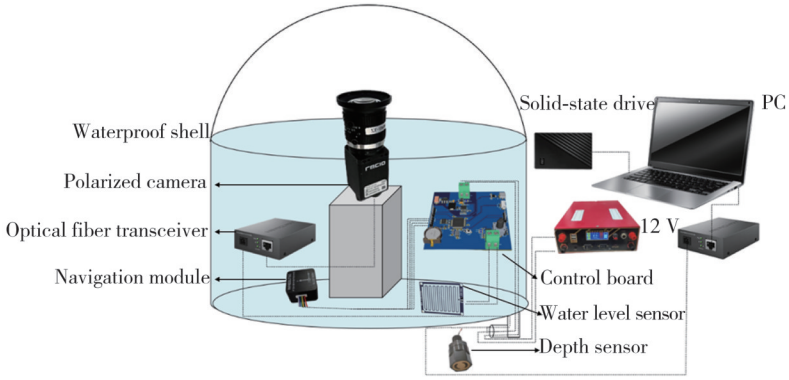

Fig. 5 Schematic diagram of acquisition device

2.2 Static experiment of water tank

On October 17, 2023, underwater atmospheric polarization patterns were measured at coordinates 36.001 8° N and 120.122 9° E. The experiment was commenced under clear weather conditions. An underwater polarization imaging device was placed into a 300 L water tank, and sky polarization images were captured. In the configuration of imaging devices, the zenithal region referred to the area directly above the polarization camera in the sky, typically located at the center of the image. The experiment was conducted at 11:00, with the water depth from the surface to the lens being 31.23 cm. The angle δ represented the deviation between the polarized camera and true north, also known as the standard heading angle. When $\alpha=0°$, $\gamma=0°$, and $\delta=10.40°$, the experimental results are shown in Fig.6.

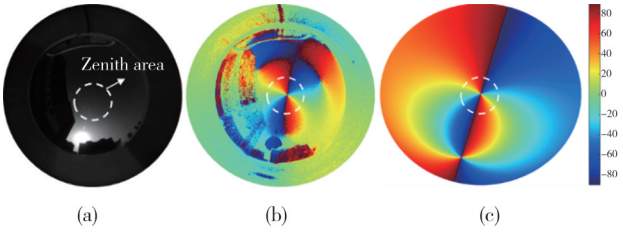

Fig. 6 Polarization distribution in static experiment of water tank. (a) Light intensity image; (b) Measured AoP image; (c) Simulated AoP image

During the time period from 11:00 to 11:30 in the morning, static experiments are conducted to capture heading data every 20 s, as illustrated in Fig.7.

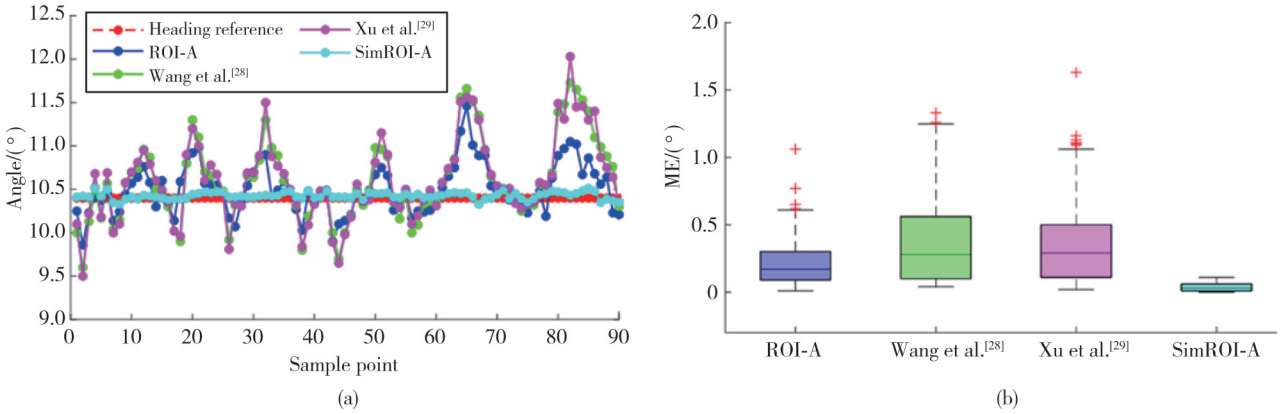

Fig. 7 Heading analysis of static experiments on water tank. (a) Heading angle error curve; (b) Maximum absolute value error

By comparing the three navigation solutions, it is observed from Fig.7(a) that the heading error of ROI-A remains the most stable. To quantitatively compare the performance of the three strategies, their maximum absolute errors were calculated. The specific results are shown in Fig.7(b) as a box plot. It was evident that the fluctuation range of ROI-A was the smallest with the least values exceeding the upper quartile, indicating the smallest error. The errors for Wang et al.[28] were the largest, while Xu et al.[29] had the most outliers. The simulated data SimROI-A exhibited no anomalies, indicating the presence of external environmental factors during the actual detection process, which affected the accuracy of the data. The RMSE of ROI-A was 0.30°, which was 39.65% and 39.31% lower than the methods proposed by Wang et al.[28] and Xu et al.[29], respectively.

2.3 Ocean experiment

To verify the practicality of the proposed algorithm in the marine environment, a static experiment in the ocean

was conducted. The experimental site was located in Qingdao (35.771 1° N, 120.097 3° E), where the weather was clear and sunny. The experiment was conducted on January 24, 2024. The data collection frequency was a multiple of the output frequency of the N100MINI inertial navigation module. The experiment was conducted onboard a vessel, with the apparatus deployed into the sea at depths of 0.98 m, 4.89 m, and 5.94 m, respectively. The azimuth angles calculated (shown in blue) are compared with those obtained from the Hong Kong observatory (shown in red), as depicted in Fig.8(c).

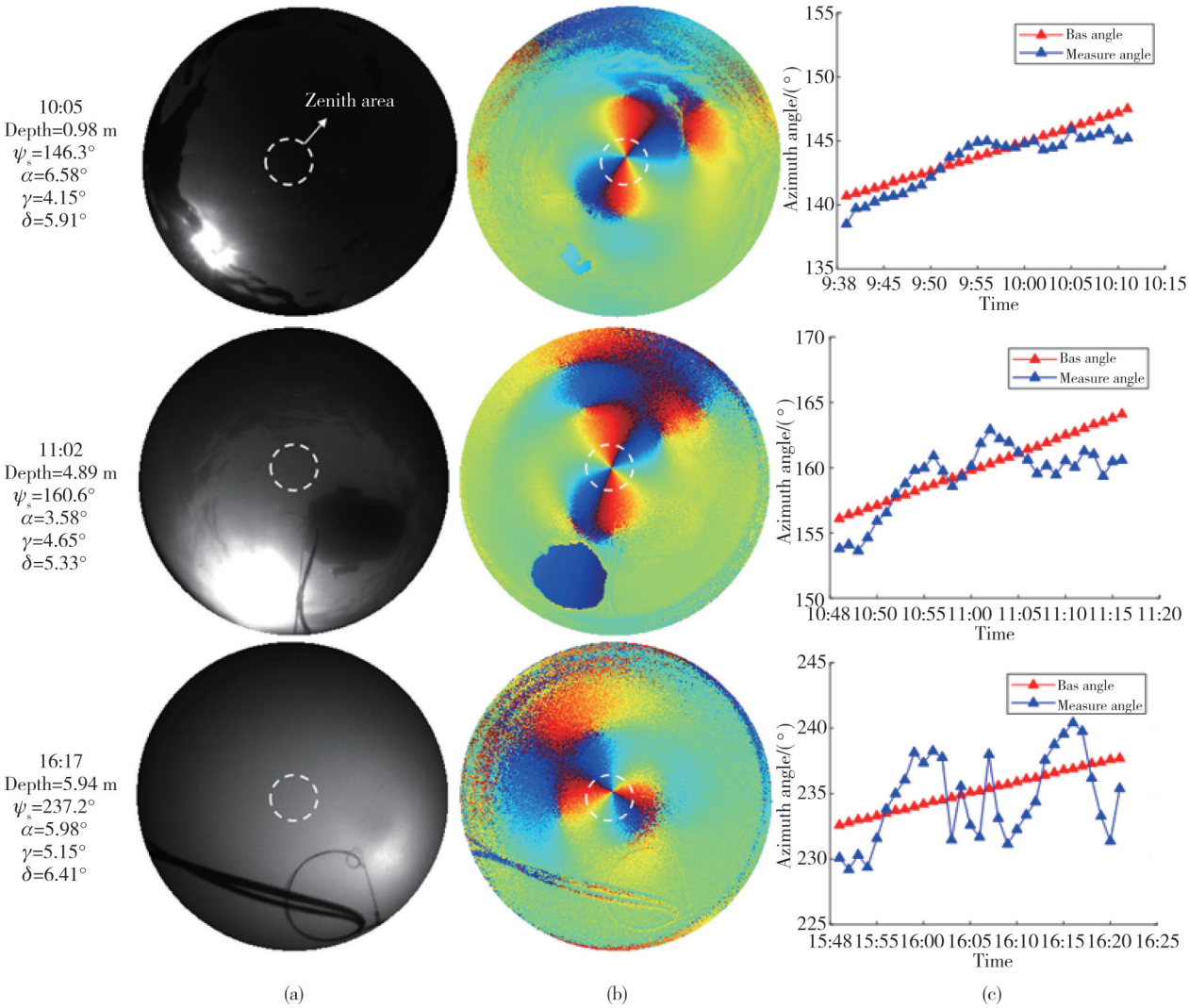

Fig. 8 Ocean experiment at different depths. (a) Light intensity images; (b) AoP images; (c) Measured and theoretical curves of solar azimuth angle at different times

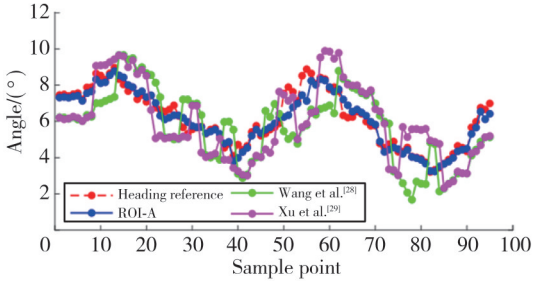

Fig. 9 Heading angle measurement results

In the oceanic environment depicted in Fig. 8, the proposed method is capable of accurately extracting the zenithal region despite continuous changes in attitude angles. Using the Hong Kong Observatory azimuth as a reference, the RMSE of the solar azimuth calculated by ROI-A at depths of 0.98 m, 4.89 m, and 5.94 m was 1.10°, 2.03°, and 3.04°, respectively. The heading measurement results at a depth of 0.98 m are shown in Fig.9, with an RMSE of 0.41°.

2.4 Discussion

The calculation of heading angles relied on the polarization information of the incident light in the zenith region. Through outdoor experiments, it was further validated that the proposed method maintained a high orientation accuracy even in situations with significant

sensor attitude tilt angles. However, with increasing depth, there was also an increasing trend in the error of the heading angles.

The proposed algorithm was based on a comprehensive analysis of the zenith region, taking into full consideration the complex effects of underwater refracted light polarization vectors. Compared with the method proposed by Wang et al. [28], the algorithm avoided excessive introduction of irrelevant information by effectively utilizing the relevant area. The method proposed by Xu et al. [29] successfully reduces redundant information in images, however, it ignores the significant influence of underwater refraction, resulting in certain constraints when processing underwater images. By integrating effective information from the zenith region, the issue of ineffective information as found in Wang et al.[28] was overcome, and the problem of neglecting underwater refraction in ROI methods was addressed. By fully utilizing the polarization information in the zenith region, higher robustness was demonstrated when facing complex environments and sensor attitude variations.

3 Conclusions

A method for azimuthal solution of zenith region light vector addition was proposed and implemented. Firstly, adaptive filtering techniques based on the attitude angles of underwater polarized imaging devices were employed to effectively extract the zenith region from polarized images, reducing computational complexity and improving accuracy. Secondly, within the extracted zenith region, the underwater refracted polarization vector was overlaid with the atmospheric polarization vector to obtain the overall polarization vector.

The experimental results demonstrated that the proposed method effectively extracted the zenith region of horizontally submerged skylight polarization images and accurately located the zenith region in inclined orientations. In both tank and ocean experiments, the heading angle's RMSE was 0.30° and 0.41°, respectively, and the solar azimuth angle was calculated in different depths of the ocean environment. A reliable and efficient solution for underwater polarization light heading estimation was provided by this approach.

In the future, the method will be tested and optimized in dynamic environments, and experiments will be conducted with varying depths under different wave conditions on the water surface to enhance the algorithm's practicality.

Acknowledgement

This work was supported by Shandong Provincial Natural Science Foundation Project (No.ZR2022MF315).

Declaration of conflicting interests

The authors have no conflict of interests related to this publication.

References

[1] YANG J, XU X, CHEN X, et al. Polarized light compass-aided inertial navigation under discontinuous observations environment. Optics Express, 2022, 30(11): 19665-19683.

[2] CHENG H, YU S, YU H, et al. Bioinspired underwater navigation using polarization patterns within Snell's window. China Ocean Engineering, 2023, 37(4): 628-636.

[3] LUO M, DANG J W. A GPS/BDS dual mode positioning algorithm for a train based on ClPSO EKF. Journal of Measurement Science and Instrumentation, 2022, 13(1): 12-20.

[4] FRANCHI M, RIDOLFI A, ALLOTTA B. Underwater navigation with 2D forward looking SONAR: An adaptive unscented Kalman filter-based strategy for AUVs. Journal of Field Robotics, 2021, 38(3): 355-385.

[5] CHOI J W, BORKAR A V, SINGER A C, et al. Broadband acoustic communication aided underwater inertial navigation system. IEEE Robotics and Automation Letters, 2022, 7(2): 5198-5205.

[6] ZHANG B, JI D, LIU S, et al. Autonomous underwater vehicle navigation: a review. Ocean Engineering, 2023, 273: 113861.

[7] WANG X, GAO J, ROBERTS N W. Bio-inspired orientation using the polarization pattern in the sky based on artificial neural networks. Optics Express, 2019, 27(10): 13681-13693.

[8] LI Q H, HU Y, HAO Q, et al. Skylight polarization patterns under urban obscurations and a navigation method adapted to urban environments. Optics Express, 2021, 29(25): 42090.

[9] PAN S, LIN J, ZHANG Y, et al. Image-registration-based solar meridian detection for accurate and robust polarization navigation. Optics Express, 2024, 32(2): 1357-1370.

[10] ZHAO H J, XU W J, ZHANG Y, et al. Polarization patterns under different sky conditions and a navigation method based on the symmetry of the AOP map of skylight. Optics Express, 2018, 26(22): 28589-28603.

[11] WAN Z H, ZHAO K C, LI Y H, et al. Measurement error model of the bio-inspired polarization imaging orientation sensor. Optics Express, 2022, 30(1): 22-41.

[12] IVANOFF A, WATERMAN T H. Factors, mainly depth and wavelength, affecting the degree of underwater light

polarization. Journal of Marine Research, 1958, 16(3): 283-307.
[13] POWELL S B, GARNETT R, MARSHALL J, et al. Bioinspired polarization vision enables underwater geolocalization. Science advances, 2018, 4(4): eaao6841.
[14] PATEL R N, CRONIN T W. Mantis shrimp navigate home using celestial and idiothetic path integration. Current Biology, 2020, 30(11): 1981-1987.
[15] PARKYN D C, AUSTIN J D, HAWRYSHYN C W. Acquisition of polarized-light orientation in salmonids under laboratory conditions. Animal Behaviour, 2003, 65(5): 893-904.
[16] SABBAH S, BARTA A, GÁL J, et al. Experimental and theoretical study of skylight polarization transmitted through Snell's window of a flat water surface. Journal of the Optical Society of America A, Optics, Image Science, and Vision, 2006, 23(8): 1978-1988.
[17] LYNCH D K. Snell's window in wavy water. Applied Optics, 2015, 54(4): B8-B11.
[18] HU P W, YANG J, GUO L, et al. Solar-tracking methodology based on refraction-polarization in Snell's window for underwater navigation. Chinese Journal of Aeronautics, 2022, 35(3): 380-389.
[19] HU P W, YANG J, QIAO J Z, et al. Underwater downwelling radiance fields enable three-dimensional attitude and heading determination. IEEE Transactions on Industrial Informatics, 2024, 20(2): 2109-2118.
[20] HU P W, LIU W B, YANG J, et al. Underwater autonomous orientation using submarine light intensity gradient. Mechatronics, 2024, 98: 103134.
[21] DUPEYROUX J, VIOLLET S, SERRES J R. An ant-inspired celestial compass applied to autonomous outdoor robot navigation. Robotics and Autonomous Systems, 2019, 117: 40-56.
[22] LIU X, YANG J, LI W, et al. Tightly coupled modeling and reliable fusion strategy for polarization-based attitude and heading reference system. IEEE Transactions on Industrial Informatics, 2022, 19(1): 62-73.
[23] LU H, ZHAO K, WANG X, et al. Real-time imaging orientation determination system to verify imaging polarization navigation algorithm. Sensors, 2016, 16(2): 144.
[24] HAN G L, ZHANG L L, HE X F, et al. A novel orientation method for polarized light compass under tilted conditions. IEEE Sensors Journal, 2020, 20(18): 10554-10563.
[25] FAN C, HU X P, HE X F, et al. Integrated polarized skylight sensor and MIMU with a metric map for urban ground navigation. IEEE Sensors Journal, 2018, 18(4): 1714-1722.
[26] GUO L, ZHAO Q, YANG J, et al. A depth-adaptive underwater polarized sun calculation method: CN116222550 B. 2023-06-06.
[27] WU X, ZHAO D, YU H, et al. Bionic polarization orientation method under severe weather. Navigation Positioning & Timing, 2022, 9(2): 104-111.
[28] WANG Y J, HU X P, LIAN J X, et al. Bionic orientation and visual enhancement with a novel polarization camera. IEEE Sensors Journal, 2017, 17(5): 1316-1324.
[29] XU J F, LI H Z, LÜ W H, et al. Design of a real-time orientation sensor based on atmospheric polarization light. Applied Optics, 2023, 62(25): 6680-6688.

水下天空偏振图像天顶区域光矢量叠加航向解算

房　政[1], 郭银景[1,2*], 孔　芳[3], 吕　雪[1], 杜春晓[1], 阮耀煌[1]

1. 山东科技大学 电子信息工程学院, 山东 青岛 266590;
2. 青岛智海牧洋科技有限公司, 山东 青岛 266590;
3. 山东科技大学 电气与自动化工程学院, 山东 青岛 266590

摘　要: 水下天空光偏振图像可以用于航向测量, 具有抗干扰、无累积误差等优点。本文提出了一种基于天顶区域光矢量叠加的水下偏振图像航向解算方法, 以获取水下环境中的航向角。该方法首先分析水下天空光偏振图像, 并结合姿态信息提取出天顶区域的偏振信息。然后, 利用叠加运算将天顶区域内的水下折射光偏振矢量与大气偏振光偏振矢量进行合成。通过对偏振矢量的最优解算, 可以精确地获取水下目标的航向角。实验结果显示, 该方法在水箱实验中航向角的均方根误差(RMSE)为0.30°, 海洋实验航向角的RMSE为0.41°; 并分别在0.98米, 4.89米和5.94米深的海洋中解算出太阳方位角的RMSE分别为1.10°, 2.03°和3.04°。

关键词: 偏振图像;航向测量;天顶区域;矢量叠加

引用格式: FANG Zheng, GUO Yinjing, KONG Fang, et al. Solution of light vector superposition heading in zenith region of underwater sky polarization image. Journal of Measurement Science and Instrumentation, 2024, 15(2): 157-165.